Bachelor Project

Czech Technical University in Prague

F4 Faculty of Nuclear Sciences and Physical Engineering
Department of Physics

Longitudinal Electron Beam stability at EuXFEL and FLASH at DESY

Roman Janovčík

Supervisor: Ing. Jiří Král, Ph.D.
Field of study: Nuclear and Particle Physics
2023

FAKULTA JADERNÁ A FYZIKÁLNĚ INŽENÝRSKÁ

KATEDRA FYZIKY

ZADÁNÍ BAKALÁŘSKÉ PRÁCE

Akademický rok: 2022/2023

Student: Roman Janovčík

Studijní program: Jaderná a částicová fyzika

Název práce: Longitudinální stabilita svazku elektronů na EuXFEL a FLASH
(česky)   v DESY

Název práce: Longitudinal Electron Beams stability at EuEXFEL and FLASH
(anglicky)   at DESY

Jazyk práce: Angličtina

Pokyny pro vypracování:

1) Úvod do urychlovačů a fyziky svazku

2) Úvod do instrumentace a měření longitudinálních vlastností svazku elektronů

3) Úvod do zpracování elektronického analogového signálu, digitální elektroniky

4) Úvod do práce s lasery

5) Práce na praktické části

6) Měření teploty a vlhkosti v systému BAM a jejich vlivu na přesnost výsledků

7) Vyhodnocení funkce měření intenzity laserového světla, odladění systému, kalibrace

8) Možné rozšíření: elektronický návrh, prototyp a výroba nového detektoru intenzity laserového světla

Doporučená literatura:

[1] W. Decking et al., "A MHz-repetition-rate hard X-ray free-electron laser driven by a superconducting linear accelerator", Nat. Photonics, vol. 14, pp. 391-397, 2020. doi:10.1038/s41566-020-0607-z

[2] Prototype of the Improved Electro-Optical Unit for the Bunch Arrival Time Monitors at FLASH and the European XFEL Hannes Dinter, et al. Part of Proceedings, 37th International Free Electron Laser Conference (FEL 2015) : Daejeon, Korea, August 23-28, 2015, DOI: 10.18429/JACoW-FEL2015-TUP049

[3] P. Schmüser et al. Free-Electron Lasers in the Ultraviolet and X-Ray Regime: Physical Principles, Experimental Results, Technical Realization. Springer Cham, 2014. ISBN: 978-3-319-04081-3

[4] Schreiber, Siegfried, and Bart Faatz. "The Free-Electron Laser FLASH." High Power Laser Science and Engineering 3 (2015): e20. doi:10.1017/hpl.2015.16.

Jméno a pracoviště vedoucího bakalářské práce:

Ing. Jiří Král, Ph.D.
Katedra fyziky, Fakulta jaderná a fyzikálně inženýrská ČVUT v Praze
German Electron Synchrotron DESY
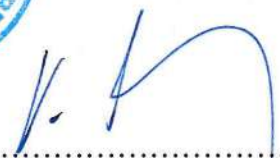
Datum zadání bakalářské práce: 20.10.2022

Termín odevzdání bakalářské práce: 02.08.2023

Doba platnosti zadání je dva roky od data zadání.

....
garant studijního programu

....
vedoucí katedry

....
děkan

V Praze dne   20.10.2022

ČESKÉ VYSOKÉ UČENÍ TECHNICKÉ V PRAZE

Fakulta jaderná a fyzikálně inženýrská

Břehová 7
115 19 Praha 1

PROHLÁŠENÍ

Já, níže podepsaný

Jméno a příjmení studenta:	Roman Janovčík
Osobní číslo:	502462
Název studijního programu (oboru):	Jaderná a částicová fyzika

prohlašuji, že jsem bakalářskou práci s názvem:

Longitudinální Stabilita svazku elektronů na EuXFEL a FLASH v DESY

Longitudinal Electron Beam stability at EuXFEL and FLASH at DESY

vypracoval samostatně a uvedl veškeré použité informační zdroje v souladu s Metodickým pokynem o dodržování etických principů při přípravě vysokoškolských závěrečných prací.

V Praze dne 1.8.2023

....

podpis

Název práce:

Longitudinální Stabilita svazku elektronů na EuXFEL a FLASH v DESY

Autor: Roman Janovčík

Studijní program: Jaderná a částicová fyzika

Druh práce: Bakalářská práce

Vedoucí práce: Ing. Jiří Král, Ph.D.
                      Katedra fyziky, Fakulta jaderná a fyzikálně inženýrská ČVUT v Praze
                      German Electron Synchrotron DESY

Abstrakt: European X-ray Free-Electron Laser (EuXFEL) a Free-electron LASer in Hamburg (FLASH), nacházející se v DESY, poskytují extrémně krátké, koherentní světelné pulzy a nabízejí jedinečné možnosti vědeckého výzkumu pro pozorování hmoty na atomové a molekulární úrovni. Přesné načasování elektronových svazků, ve kterém hrají zásadní roli Bunch Arrival Monitory (BAMy), je pro jejich provoz důležité. V této práci byl analyzován vliv šumu optického spínače na přesnost algoritmu čtení BAM signálu a vliv podmínek prostředí na měření doby příletu svazku. Změny teploty a vlhkosti byly měřeny na urychlovačích EuXFEL a FLASH. Výsledek měření nabízí vhled do stability měření doby příletu svazku vůči změnám prostředí. Termoelektrický (TEC) regulátor teploty dokáže stabilizovat teplotu s přesností 0,001 K v BAMu. V této práci je také představen nový design pin headru pro TEC regulátor.

Title:

Longitudinal Electron Beam stability at EuXFEL and FLASH at DESY

Author: Roman Janovčík

Abstract: The European X-ray Free-Electron Laser (EuXFEL) and the Free-electron LASer in Hamburg (FLASH) located at the German Electron Synchrotron (DESY) provide extremely short, coherent, laser-like pulses, and offer unique scientific research opportunities for matter imagining at atomic and molecular levels. Precise timing control of electron bunches, in which Bunch Arrival Monitors (BAMs) play a vital role, is important for their operation. Influence of an optical switch noise on the precision of BAM signal readout algorithm was analysed in this project, together with influence of environmental conditions on bunch arrival time measurement. Temperature and humidity measurements were conducted at the EuXFEL and FLASH accelerators. Their results offer an insight into the bunch arrival time measurement stability against environmental conditions. The Thermo Electric Cooling (TEC) Temperature Controller can stabilize temperature with 0.001 K precision in the BAM. A new design of a TEC controller pin header is also presented in this project.

Acknowledgements

Contents

Figures

xiv

Tables

Chapter **1**

Preface

Particle accelerators offer numerous research opportunities in various scientific disciplines. A brief overview of their development, accelerator physics, instrumentation and applications is provided in Chapter 2.

The European X-ray Free-Electron Laser (EuXFEL) and the Free-Electron LASer in Hamburg (FLASH) located at the German Electron Synchrotron (DESY) in Hamburg provide extremely brief, coherent, high brilliance light pulses able to probe matter at atomic and molecular resolution. [1] Chapter 3 describes the process of synchrotron light production in Free-Electron Lasers and their development.

For production of stable, extremely short laser pulses a precise femtosecond timing control of electron bunches, provided by Bunch Arrival Monitors (BAMs), is needed. The working principle and layout of the BAMs are the focus of Chapter 4.

Chapters 5, 6 and 7 focus on the practical part of this project. The influence of noise induced by an optical switch on the BAM signal computation algorithm is shown in Chapter 5.

The effect of varying temperature on the arrival time measurement is discussed in Chapter 6 together with a new design of a pin header PCB for a Thermo-Electric Cooling (TEC) Temperature Controller, which provides precise temperature stabilization of 0.001 K.

Chapter 7 discusses the relative humidity fluctuations inside the BAMs, and describes calibration of the humidity sensors used for the measurement.

A summary of the project contents and results is given at the end, together with future outlooks.

Chapter 2

Introduction to accelerator physics

2.1 Accelerator development

According to Oliver Bruning [2] two key physics discoveries motivated the development of particle accelerators: Rutherford's 1919 discovery that bombardment of Nitrogen atoms with alpha particles from radioactive decay can disintegrate the Nitrogen nucleus and Einstein's famous equation $E = mc^2$ from 1905.

2.1.1 Electrostatic accelerators

Rutherford expressed the need for devices capable of supplying charged particles with enough energy to disintegrate atomic nuclei at the Royal Society in 1927. [3] Rutherford's plea lead to the development of electrostatic accelerators. In 1928 Gamov predicted quantum tunneling and estimated that an energy of 500 keV might be enough to split an atom. [4] Cockroft and Walton have disintegrated a Lithium atom in 1932. [2] The Cockcroft–Walton Generator utilized a series of capacitors and diodes. In 1929 the first working model of the Van de Graaf generator has been built which utilized a moving silk belt to accumulate charge on a metal sphere. Improvements of the Van de Graaf generator lead to the creation of Tandem accelerators and Pelletrons. [5]

▪ 2.1.2   Linear accelerators

In 1925 G. Ising proposed the idea of a particle acceleration using alternating radio-frequency fields, and in 1928 R. Wideroe, inspired by Ising, accelerated Potassium ions to an energy of 50 keV using a drift tube linear accelerator. [6] In 1937 Russell and Sigurd Varian invented the klystron – a device capable of amplifying high radio-frequencies. [3]

▪ 2.1.3   Cyclotrons

E. Lawrence saw Wideroe's drift tube design and together with S. Livingston built the first Cyclotron, measuring just 5 inches in diameter, in 1931. The Cyclotron works by supplying radio-frequency voltage to two D-shaped plates, called dees, in a constant magnetic field. The particles are accelerated while passing a gap between the dees. [6] Special relativity imposes limitations on the achievable energies in a Cyclotron. Synchrocyclotron changes the frequency of the acceleration voltage, while Isochronous cyclotrons use varying magnetic fields. [2]

▪ 2.1.4   Betatrons

Betatrons are induction accelerators working as transformers. The primary coil is a magnet system, while the beam serves as the secondary coil. The first concept of a Betatron was developed by Wideroe and J. Slepian. [2] In 1940 D. Kerst built the first Betatron, and in 1941 D. Krest and R. Serber solved the transverse stability problem of Betatron oscillations. [6]

▪ 2.1.5   Synchrotrons

The magnetic field in synchrotrons guides the particles on a closed orbit. Because the energies and arrival times of particles in the radio-frequency cavities deviate from the idealized synchronous particles, focusing is needed. [7] In 1944 V. Veskler and E. McMillan independently discovered the principle of phase stability and invented the synchrotron. [4] In 1952 the first weak focusing synchrotron, the Cosmotron, was built at Brookhaven National

Laboratory. The same year E. Courant, M. Livingston and H. Snyder proposed strong focusing. Smaller magnets could be used and higher beam energies achieved. [7] The total central-mass energy in a fixed target collision includes only a fraction of particle's energy, whereas in a head-on collision the energy of both particles is available. [4] B. Touschek built the first storage ring in 1960 and the first proton-proton collider, the Intersecting Storage Rings, was completed in 1969. [6]

2.2   Basic components of accelerators

As was briefly mentioned in section 2.1.1 the main reason for accelerator development is to deliver particles of desired kinetic energy. The Lorentz equation (2.1) expresses the force acting on a particle with charge $e = 1.602 \cdot 10^{-19}$ C and velocity $\vec{v}$ in an electromagnetic field expressed by electric field strength $\vec{E}$ and magnetic flux density $\vec{B}$ as

$$\vec{F} = e(\vec{E} + \vec{v} \times \vec{B}). \tag{2.1}$$

Since the Lorentz force is perpendicular to the magnetic field, particle acceleration can occur only by utilising electric fields. The energy of a particle with charge q placed in a potential difference V is $E = qV$, thus the standard unit of energy in particle accelerators is an electron-volt (1 eV $= 1.602 \cdot 10^{-19}$ J). Instead of a static DC voltage most modern accelerators utilise time-varying, oscillatory resonant cavities. [8]

Resonant cavities usually operate with resonant frequencies in the radio-frequency (RF) part of the electromagnetic spectrum, and are thus called RF cavities. Instead of a continuous beam of particles RF cavities provide bunched beams since the particles have to arrive at the cavity when the electric field strength has the highest value in the direction of the particles' motion. The accelerating gradient of normal-conducting RF cavities is mainly limited by the heating of the walls causing deformation of the cavity, RF breakdown – when plasma can be formed inside the cavity due to vaporization and ionization of the walls, and power limits and operating costs. Circular accelerators such as cyclotrons, described in section 2.1.3, and synchrotrons, described in section 2.1.5 use magnetic fields to repeatedly deliver the particle beam to the RF cavities to better utilise their limited accelerating gradient. [8]

Magnets are used to bend the trajectory of particles and also to focus particle beams. Dipole magnets bend or correct the trajectory of particle beams. Multipole magnets, such as quadrupole and sextupole magnets, focus the beam inside of the center of the chamber, analogous to optical lenses

focusing light into a focus point. Quadrupole magnets focus the beam either horizontally or vertically while defocusing it in the other direction. However this issue is solved by installing another quadrupole magnet rotated by 90° since the combined effect of a focusing and defocusing results in overall focusing of the beam. [8]

Vacuum chambers are metal pipes inside of which the particle beams travel. The chambers have to be kept in ultra high vacuum in order to avoid collisions of particles with air molecules.

Electron guns produce the initial electron beam which is then accelerated using RF cavities through different methods. One method is by thermionic emission in which the electrons gain enough energy to overcome the energy gap and escape from the surface of the material. Other method is using photocathodes to generate electrons from light through photelectric effect. The main value used to express the quality of a photocathode is quantum efficiency, QE, which is defined as the ratio of the number of produced electrons to the number of incident photons. [9]

Kickers and septa guide the injected beam into a synchrotron. A septum separates the injected beam from the stored beam via two electric or magnetic fields. One ideally homogeneous, the other a low fringe field in order to not affect the beam in the storage ring. A kicker is capable of quickly deflecting the beam during injection or extraction. [10]

Emittance ϵ describes the area in the phase space of a particle beam. The coordinates of the phase space are the position of the particle and its derivative. Liouville's theorem states that the local density of the points in phase space corresponding to particles inside of a beam is constant. According to this theorem emittance of a particle beam, on which only conservative forces act, is a conserved quantity. The quantity which describes the application performance, and thus needs to be maximized, of an electron accelerator is the brightness B which can be expressed as

$$B = \frac{N_e}{\sigma_{nx}\sigma_{ny}\sigma_{nz}}, \qquad (2.2)$$

where N_e is the number of electrons inside the beam and σ_{nx}, σ_{ny} and σ_{nz} are the horizontal, vertical and longitudinal normalized beam emittances respectively. Normalized emittance represents the area in a phase space, with particle beams position and momentum as its coordinates, and can be expressed as $\epsilon_n = \gamma\beta\epsilon$, where $\beta = \frac{v}{c}$ and $\gamma = \frac{1}{\sqrt{1-\beta^2}}$ is the Lorentz factor. [9]

■ 2.2.1   Instrumentation and diagnostics

To monitor the properties of particle beams numerous instrumentation devices and beam diagnostics are placed along the vacuum chamber of the accelerators. Some are described here:

- **Beam Position Monitors (BPMs)** serve as non-destructive diagnostics which determine the centre of mass position of charged particle beams. BPMs measure the transverse position of the beam, but can also measure the charge of the beam. The passing charged particle bunches induce electrical signal in pick-ups, producing AC signal. These electromagnetic pick-ups can be constructed as buttons, striplines or rings. [11]

- **Beam Loss Monitors (BLMs)** determine the amount of particles the beam has lost. BLMs are mounted outside the walls of the vacuum chamber. To detect the particle showers created in the walls of the chamber by the lost beam particles BLMs utilise either ionisation chambers, proportional counters, Geiger counters or scintillation detectors, etc. There are two types of beam losses: irregular and regular. Irregular beam losses are avoidable and often result from a misaligned beam or faulty accelerator components. Usually well designed collimator systems, which can direct scattered particles into a parallel trajectory, are able to capture most of the losses, but some can still cause damage in other parts of the accelerator. Generally, misaligned beams are dumped via an accelerator beam dump. Regular beam losses are typically not avoidable and usually occur near collimator structures. [12]

- **Beam Current Monitors (BCMs)** measure the intensity, i.e. the charge of the beam. Measurement of the beam current can be also used to determine lifetime of the beam and the machine safety inside of storage ring or superconducting linacs. The current is typically measured by a current transformer in DC current transformers (DCCTs) or integrated current transformers (ICTs) which can measure the charge of a bunch of duration between 1 ps and 1 μs. An insulating gap in a Wall Current Monitors (WCM) forces image currents in the chamber walls to pass a belt of low inductance and signal is collected by circumferentially positioned resistors. The WCM can be also be used as a BPM for bunch lengths comparable to the dimension of the WCM. Faraday cups stop the beam completely, thus the beam loses all of its energy to the cup, and the accumulated charge is converted to current. [13, 9]

■ 2.3 Application of accelerators

The driving force of accelerator research development has mainly been high energy and nuclear physics. However synchrotron radiation research may even outnumber that in high energy physics. The X-ray and UV light is used to reveal the structure of protein or enzyme molecules, surface layers of catalysts and crystal materials in semiconductors. Other industry usage of accelerators includes production of radioisotopes, cancer therapy, material analysis, electron beam welding, chip production, ion implantation, oil and gas extraction, national security, food sterilization, archaeology and art examination. [5, 14]

■ 2.3.1 Synchrotron light sources

As described in section 2.2, synchrotrons use bending magnets to send particle beams through an accelerating cavity multiple times. However the beams loose energy on a circular trajectory in form of synchrotron radiation. This radiation was an unwanted effect at first, but later found use in a multitude of applications mentioned in section 2.3.

Synchrotron light was first discovered in 1947 at an electron synchrotron. Synchrotron radiation sources are classified into generations. The first generation consists of storage rings operating in the parasitic mode to existing high energy electron-positron colliders. Dedicated low-emittance light sources are used in the second generation. The third generation comprises insertion devices, producing high-brilliance photon beams, using dedicated high-brightness electron beams. The current, fourth generation, comprises of linac driven free-electron lasers, which are discussed in the next chapter. [6]

Chapter 3

Free-electron lasers

Free-Electron Lasers (FELs) generate brief, coherent and high brilliance light through the interaction of high energy electrons with magnetic field. [1] Electrons produce synchrotron radiation in the bending magnets of high-energy accelerators. For Lorentz factor $\gamma >> 1$ the radiation is emitted nearly tangentially to the orbit of the electrons. In modern synchrotron light sources the electrons undergo sinusoidal motion inside of an undulator of dipole magnets with alternating polarity. The electrons emit nearly monochromatic undulator radiation concentrated in a narrow angular cone with an opening angle of $\pm\frac{1}{\gamma}$. The wavelength of the undulator radiation λ_l is given by the equation

$$\lambda_l = \frac{\lambda_u}{2\gamma^2}\left(1 + \frac{K^2}{2}\right), \quad K = \frac{eB_0\lambda_u}{2\pi m_e c} \approx 1, \tag{3.1}$$

where λ_u is the period of the undulator array, K is the undulator parameter and B_0 is the magnetic field of the undulator. [15] In FELs the power and coherence of the undulator radiation is increased through the process of Self Amplified Spontaneous Emission. The emitted radiation moves faster than the electrons, interacting with electron bunches further up, resulting in exponential increase in power and coherence. [16]

Conventional lasers consist of three main parts – a laser medium, a pump and a resonator. In FELs the role of the medium and the pump is served by the electron beam. For wavelengths below 100 nm resonators are not feasible, instead the SASE process actualizes the laser gain through a single passage in the undulator array. Main advantage of FELs over conventional lasers is their tunability across a wide range of wavelengths which, as can be seen from equation (3.1), depend on the energy of the electron bunches. [15]
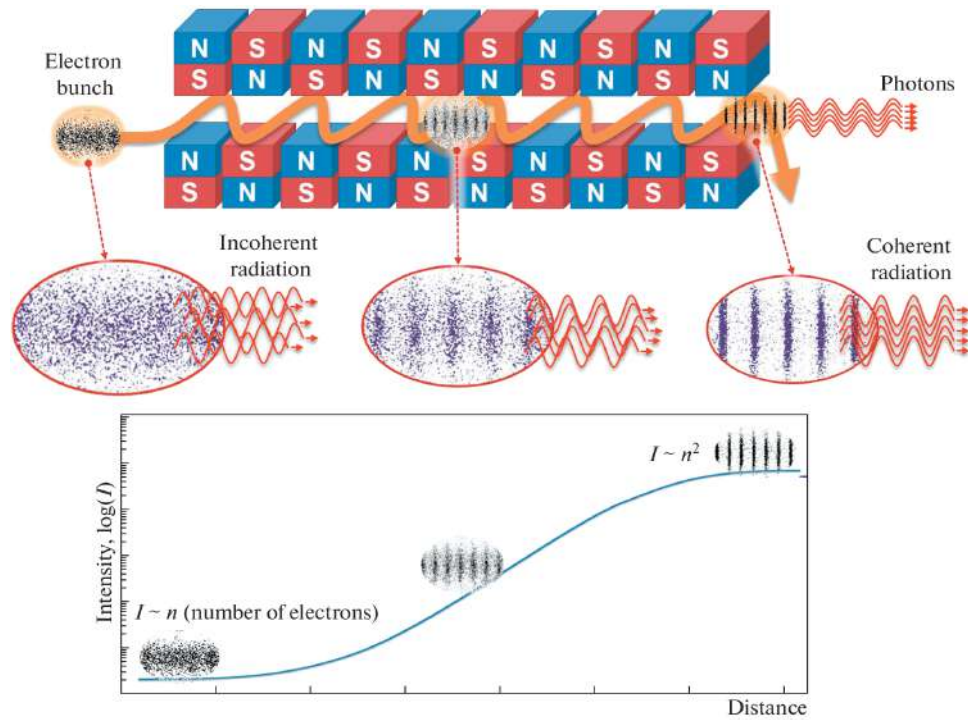
Figure 3.1: Schematic view of the undulator and the formation of micro-bunches in the SASE process. The intensity of the radiation increases exponentially with increasing length of the undulator. Image taken from [17].

Low gain FELs equipped with an optical cavity produce radiation in the THz, infrared and visible wavelength spectrum. [7] High gain FELs rely on the SASE process, produce light in the UV and X-ray spectrum, and operate on the principle of micro-bunching – electrons which lose energy to the light wave travel on a cosine trajectory of larger amplitude than the electrons which gain energy from the light wave. The micro-bunch formation can be seen in Fig. 3.1. The charge of the electron bunch, before entering the undulator, is uniformly distributed. However through light emission by more energetic electrons and absorption of this light by less energetic electrons the charge density inside the bunch is modulated, resulting in the creation of micro-bunches. Since the phase space available to the photons emitted by micro-bunches is reduced, the produced radiation is nearly coherent, while the intensity is proportional to the square of the number of electrons. [15] The electron bunches are dumped at the end of the undulator while the radiation is guided by photon beamlines to experimental stations.

3.1 Development of FLASH and EuXFEL

The principle of a free-electron laser was first described by John Madey in his work *Stimulated Emission of Bremsstrahlung in a Periodic Magnetic Field* [18] published in 1971. John Madey and his group at Stanford constructed the first FEL using an optical cavity operating in the infrared wavelength region. The theory of single-pass X-ray FELs was devised soon after. At the German Synchrotron (DESY) the TESLA Test Facility Free-Electron Laser (TTF FEL) started construction in 1995. The TTF FEL focused on building a superconducting linear accelerator combined with a FEL in the VUV–XUV regime. The facility was named FLASH in 2006. [1]

The Free Electron LASer in Hamburg (FLASH), which started user operation in 2005, is the first FEL operating in the XUV/soft X-ray regime. The radiation pulses in the 4.1–47 nm wavelength range are about 10–50 fs long with peak power of several GW. The FEL is driven by a 315 m long superconducting linear accelerator with electron beam energy of up to 1.25 GeV, and has two SASE beam lines. [16, 19]

FLASH could be considered the prototype of the European X-ray Free Electron Laser (EuXFEL) which started user operation in 2017. [1] EuXFEL is a 3.5 km long FEL based on a 17.5 GeV superconducting linear accelerator, and can produce up to 27 000 electron bunches per second using a 10 Hz RF pulse repetition rate of 600 μs duration for three SASE beam lines. [20, 21]

3.2 Bunch compression and stabilization

Because the electron bunch density of the bunches entering the undulator is randomly distributed and the light emission is spontaneous, the SASE is a stochastic process. The pulses created by the SASE process thus contain statistical noise. To better the precision of these pulses external seeding by a laser can be used to improve the quality of the radiation. Or, before reaching a saturation point, the FEL radiation can be used as a self-seeding laser to the electron bunches which are redirected to another undulator by a process called „debunching". However to increase the timing precision, precise arrival time control of the driving electron bunches at the undulator is needed, which requires accurate bunch arrival time stabilization in the superconducting linac of the FEL.
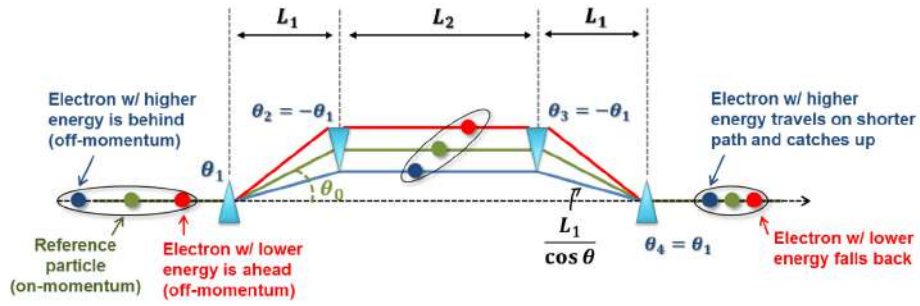
Figure 3.2: Schematic view of a four-dipole bunch length compressor magnetic chicane and particles' motion through it. Image taken from [23].
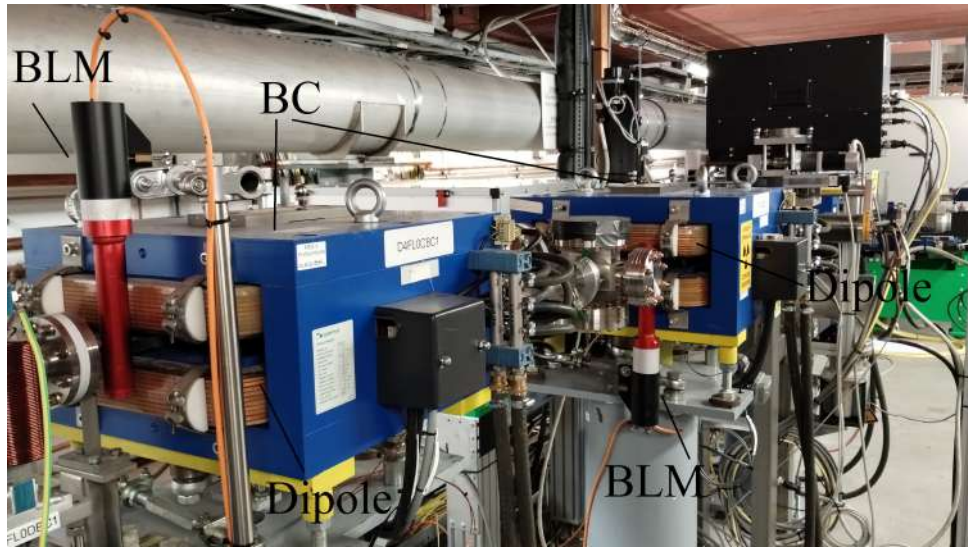
Figure 3.3: Image of accelerator components, such as Bunch Compressor (BC) dipoles and Beam Loss Monitors (BLM), taken at the FLASH facility.

Timing fluctuations occur at various points in the accelerator. However the main contribution to the timing fluctuations is due to the dispersive effects of bunch compressor chicanes, which are needed to generate high electron bunch densities. [22, 15] Dipole bunch compressors at the FLASH linac can be seen in Fig. 3.3 together with Beam Loss Monitors, consisting of a scintillator and a photomultiplier tube. The compression of the electron bunches is needed to produce the extremely short FEL laser pulses. The FEL laser pulses also need to have high brilliance which, as seen from equation (2.2), means small emittance is needed. However, due to the repulsive effects of the Coulomb force, the transverse emittance of the beam increases for high beam currents. To preserve the small beam transverse emittance, the electron gun photocathode generates low current beam, which is then increased through bunch compression inside bunch compressor magnetic chicanes. The magnetic chicanes, shown in Fig. 3.2, use four dipole magnets of bending angles θ_1, $-\theta_1$, $-\theta_1$, θ_1, and are separated by distances L_1, L_2 and L_1. [23] The magnetic chicanes compress and stabilize the electron bunches in the longitudinal

direction while increasing the beam current, however they also introduce bunch arrival time fluctuations based on variations in the energy-dependent path lengths. [22]

The precise bunch arrival time control is realised through optical synchronization using a pulsed near-infrared laser in length-stabilized optical fibres along the accelerator. [22, 24] Bunch Arrival Monitors employ such an optical synchronization scheme to determine the arrival time of electron bunches, and are discussed in the next chapter.

Chapter 4

Bunch Arrival Monitors

Bunch Arrival Monitors (BAMs) employ ultra-short pulsed laser to measure the intra bunch-train arrival time. Bunch Arrival Monitors consist of three parts, a Radio-Frequency (RF) pick-up, an Electro-Optical unit and a Data-acquisition (DAQ) and Control unit. A Master Laser Oscillator (MLO) is used to synchronize the signal from the RF unit which is then sent to the DAQ unit. [25] Fig. 4.1 shows the optical synchronization via the MLO for the BAM stations at the EuXFEL facility.

4.1 RF pick-up

The electron bunches produce signal in the Radio-Frequency unit which comprises four cone-shaped broadband pick-ups, depicted in Fig. 4.2, two opposite of each other to reduce fluctuations in the transverse direction. The bipolar signal from the RF pick-up, processed by combiners, is transmitted via coaxial cables in to a Mach–Zender type Electro-Optical Modulator (EOM) where it is probed by the reference laser from the MLO.[27]
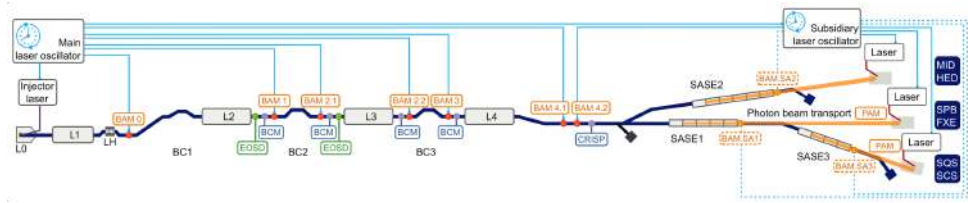
Figure 4.1: Optical synchornization of the BAM stations at the EuXFEL. Image taken from [26].
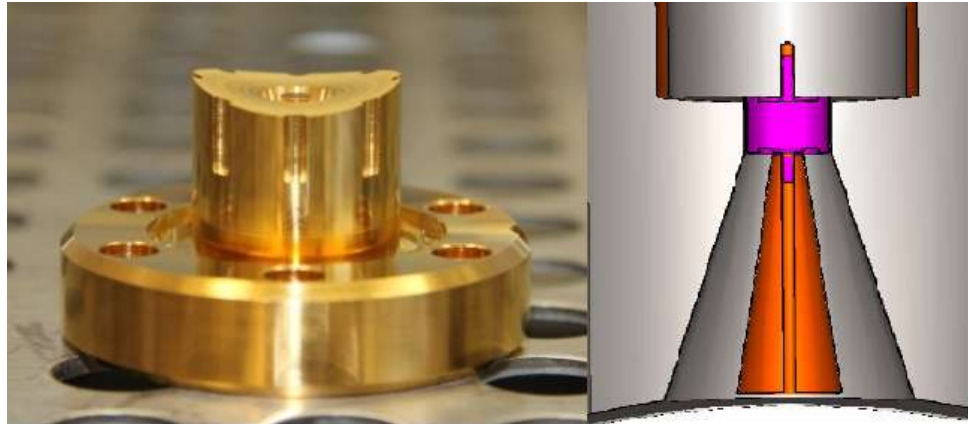
Figure 4.2: Cone-shaped RF pick-up (on the left) and its original design for the EuXFEL (on the right).

4.2 Electro-Optical unit

The Electro-Optical unit provides optical modulation of the RF signal, as well as clock signal to the DAQ unit. [25] The upper and lower compartments of the Electro-Optical unit, housing all the optical components and electronics described in this section, are shown in Fig. 4.3.

4.2.1 Electro-Optical Modulator

The E-O Modulator (EOM) encodes bunch arrival time information, collected by the RF pick-ups, into a laser pulse provided by the MLO through electro-optical intensity modulation. It functions as a Mach–Zender Modulator (MZM), splitting the laser pulse into two symmetrical branches, and applying a phase shift to them which results in amplitude modulation after their recombination through interference at the end of the EOM. The phase shift is introduced by changing the refractive index of the two beams' optical paths. The refractive index is a function of the electric field applied to the

16
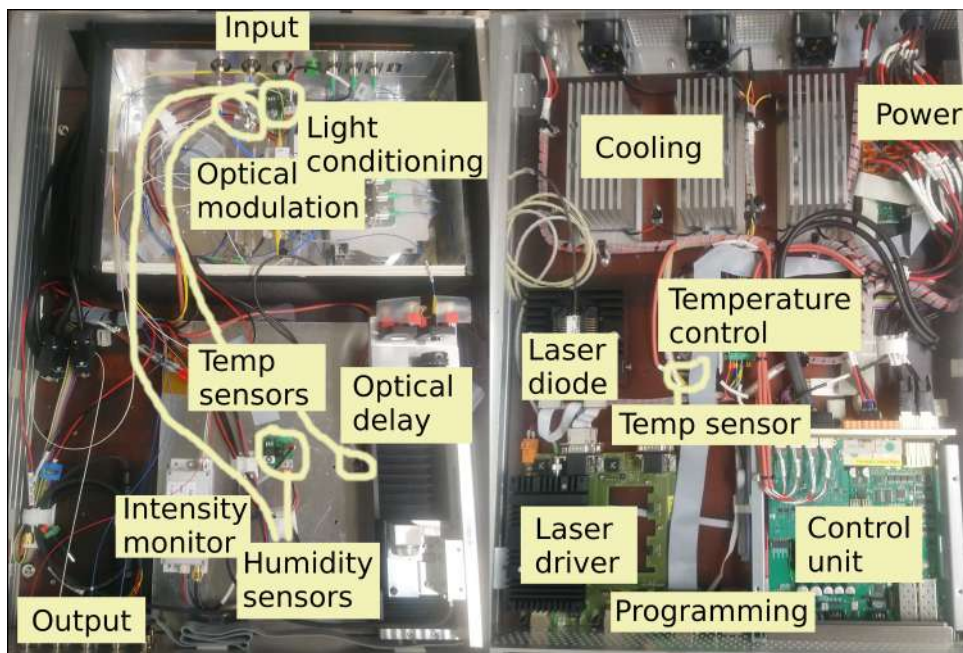
Figure 4.3: The upper (on the left) and lower (on the right) compartments of the Electro-Optical unit.

optical path by electrodes connected to the RF pick-ups. For one of the beams additional phase shift is also introduced by applying a DC bias voltage that can shift the interference pattern. [28] The laser pulses have a FWHM of approximately 1 ps and a period of 4.6 ns. The distance between two peaks of the RF signal is in the order of 10 ps while ringing of the signal can be in order of 10 ns. [25] The transmission function of the EOM, shown in Fig. 4.4, depends on the applied voltage. The voltage bias is usually set so that when there is no RF signal 50 % of the laser pulse signal is transmitted, this point is called the working point. However when the RF voltage exceeds a certain threshold, the signal becomes over-modulated and shifted by a period corresponding to a 2π phase shift of the laser pulse where further measurements do not provide meaningful results. The region, where the transmission function is monotonic for the applied voltage, is called dynamic range. [29, 30]
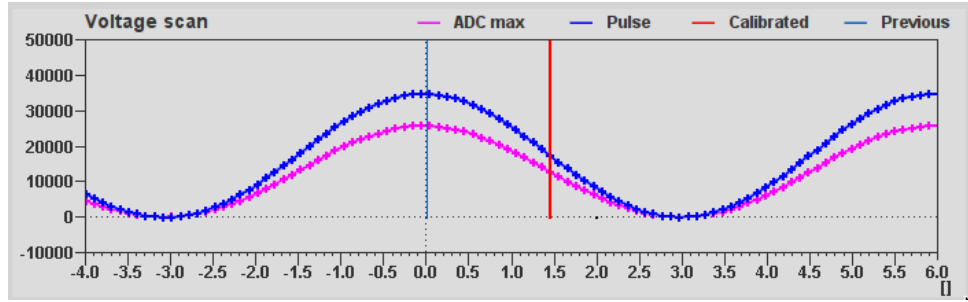
Figure 4.4: The transmission factor of the EOM as a function of applied voltage repeating with period of approximately 5 V. The red vertical line represents the working point of the EOM.

4.2.2 Optical Delay Line

To expand the dynamic range of the EOM, as well as to set the working point and calibrate the EOM, a bidirectional optical delay line (ODL) is employed. The time delay is adjusted by retroreflectors mounted onto a stage driven by a stepper motor which can change the optical path length. The distance traversed by the stopper motor corresponds to the expanded dynamic range. [29]

4.2.3 Optical switch

One macropulse bunch-train comprises multiple beam regions, depicted in Fig. 4.5, that may produce signals with distinctive timing in the RF pick-ups, and thus drive the transmission function of the EOM out of the dynamic range which leads to over-modulation. The time distance between two beam regions in one macropulse is typically 50 μs which exceeds the speed of the ODL's stepper motor. In order to switch between the beam regions two separate ODLs are used. Switching between the ODLs is realised by a fast bidirectional optical switch. The switching time is around two to three orders of magnitude lower than the time distance between the two beam regions. [25, 29]
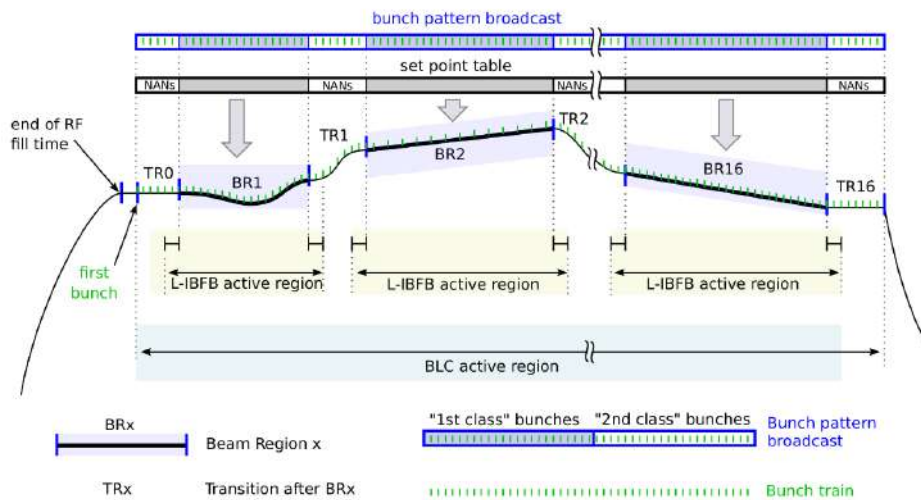
Figure 4.5: Schematic view of beam regions (BRs) and transmission regions (TRs). Image taken from [31].

4.2.4 Electronics

The main control and monitoring electronic boards inside the Electro-Optical unit are listed here:

- **Temperature Monitoring and Control Board (TMCB)** This board provides readout of several temperature and humidity sensors, as well as an interface of two temperature controllers. The board also provides control of the ODL's stepper motor, and allows to set the voltage bias in the EOMs. [25] It is a versatile FPGA board containing 14 diverse ADC and 10 DAC channels in addition to 20 configurable General Purpose Inputs and Outputs (GPIOs). It operates in stand-alone mode and provides interface via Ethernet or optical fiber. [29] Fig. 4.6 shows the TMCB with a programmable FPGA and a connector which provides analog input for two humidity sensors.

- **Laser Diode Driver (LDD)** This board serves as a high-precision, low-noise current source for the laser diodes used to amplify laser pulses. It contains a carrier and a compact mezzanine form factor, which provides an Ethernet and a CAN bus interface, and operates in stand-alone mode. [25, 29]

- **Fuse Relay Board (FRED)** This board allows remote control and monitoring of up to 8 DC voltage channels with individual fuses and current limitations for each of them. It operates in stand-alone mode with an Ethernet interface. [25, 29]
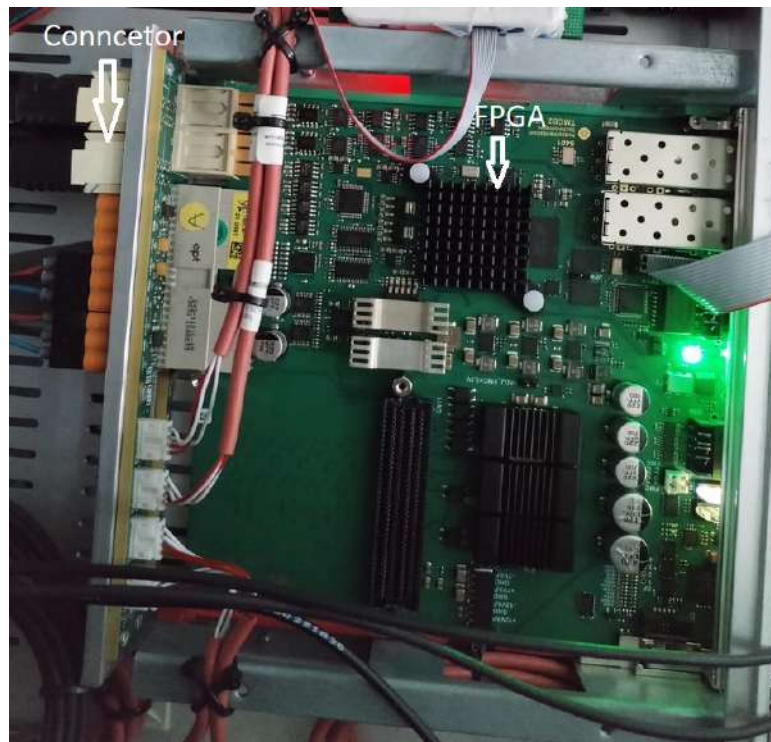
Figure 4.6: Picture of the TMCB with an analog input connector taken at DESY.

▪ **Thermo-Electric Cooling (TEC) Temperature Controller** uses
the Peltier effect to control temperature on a metallic base plate, on which
all parts are fixed. The temperature can be stabilized with precision of
up to 0.001 K. Communication with the TEC controller occurs via the
RS232 protocol using digital pins on the TMCB.

4.3 DAQ unit

The DAQ unit uses a setup based on the compact and modular Micro
Telecommunication Computing Architecture (MicroTCA), which is a standard
in Telecommunication. MicroTCA utilises a PCI Express interface, which is
its main advantage over the previously used Versa Module Europa (VME). [32]

■ 4.3.1 Firmware

The clock signal and the modulated laser pulses from the EOMs are coupled to the DAQ unit via three photodiodes, contained in a dual mezzanine DFMC-DSBAM board equipped with a clock distribution chip and four 16 bit ADCs. One ADC samples the peak and another the base. The sampling of any desired point along the laser pulse is accomplished by applying a delay to the clock via the clock distribution chip, which also performs clock synchronization, at the same rate as the rate of the laser pulses,
i.e. 216 MHz. For each macropulse 1024 of the unfiltered samples are stored usually starting from the trigger, which is provided by the X2Timer board via the backplane of the MTCA crate, but an arbitrary delay can be applied. These data are referred to as raw data. The sampled data from the ADCs are filtered according to the settings of the macropulse, such as the bunch repetition rate and bunch number, in order to obtain the modulated laser pulses and specific unmodulated ones used later for normalization of the pulse height, defined as the difference between peak and base of the laser pulse. The firmware in the FPGA provided by a DAMC-FMC25 carrier board equipped with second FPGA for board management and some additional diagnostics performs mathematical operations, such as division, on the filtered data. Both the raw and filtered data are stored in an internal RAM and then sent through a DMA to the DAQ Computer. [25]

■ 4.3.2 Feedback

To improve beam stability the beam parameters are used as feedback to the corresponding RF station. The slow RF feedback, with maximum frequency of 10 Hz, is used to compensate for induced drifts due to environmental influences, as well as regulate the RF station itself. [32] The fast beam based feedback, used for compensating stochastic fast fluctuations from pulse to pulse, is accomplished by sending the non-calibrated value of the arrival time via optical link to the Low Level RF System. The mathematical operations for the fast feedback are time critical and must be performed at the firmware level. [25]

■ 4.3.3 Software

The DAQ software is written using the DOOCS control system library. Dedicated DOOCS servers are implemented for the LDD, the BAM box man-

agement, the power management, the readout and the stepper motor server. The servers are used to read data from FPGAs, run algorithms for setting of ADCs, store data and perform calibration of the modulated signal amplitude to arrival time. [25]

Chapter **5**

Optical switch noise measurement

This chapter focuses on whether the switching of the optical switch, described in section 4.2.3, influences the precision of the algorithm for BAM signal computation, and, if that is the case, on determining the time scale of this effect, since it is important for diagnosing the different beam regions.

To get the BAM signal, first amplitude is obtained by subtracting the base signal from the peak. Then, in order to obtain the normalized amplitude of the signal, the modulated amplitude samples are divided by specific unmodulated ones. [32]

The optical switch, used in a laboratory BAM, was connected to one ODL through an optical fiber link while the other output was disconnected. At the start of the measurement the laser was switched off, and after some time the laser was switched on, which corresponds to a peak seen in Fig. 5.1.

The raw data, described in section 4.3.1, were collected from the ADCs via the mtca4u python package together with the pre-ADC signal, which was used as a reference. The 1024 raw data samples are stored in one value per ADC channel sub-array rows, and thus they need to be transposed first. The peak signal was stored in channel 0 while base signal in channel 1 of the ADC. Normalization of the amplitude was done by dividing every raw data sample by the previous one. Therefore the resulting number of samples is 1023 instead of the original 1024. The reference signal samples were calculated analogously after a single measurement.
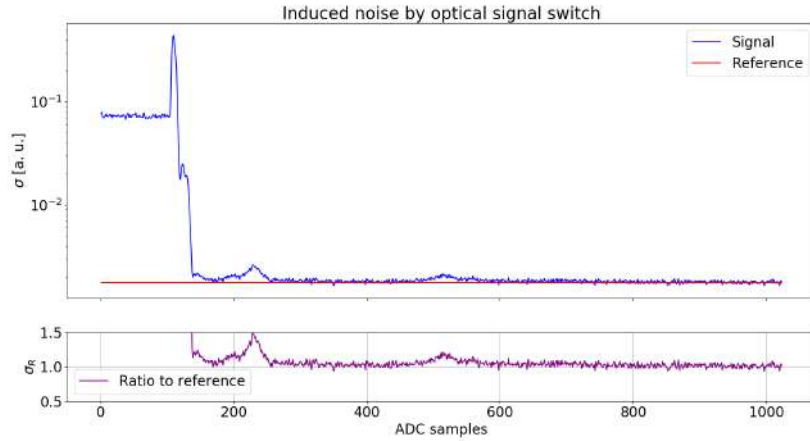
Figure 5.1: Standard deviation σ of the 1023 measured ADC samples over a certain period of time and the standard deviation σ of the pre-ADC samples used as a reference together with a ratio of these deviations.

Fig. 5.1 shows the standard deviation of the 1023 measured ADC samples over a certain period of time and the standard deviation of the 1023 reference samples together with a ratio of these deviations. As seen from Fig. 5.1, the noise induced by the optical switch influences approximately 800 ADC samples. The sampling frequency is equal to the frequency of the MLO pulses, i.e. 216 MHz, which means that the noise propagation takes up to approximately $\frac{800}{216\,\text{MHz}} = 3.7\,\mu$s. Since this time is smaller than the transition period between two beam regions, which is typically 50 μs [25], the noise introduced by optical switch to the algorithm for computing BAM signal does not affect the arrival time of bunches measured in different beam regions. Based on this measurement, the switching point between the start of one beam region and the end of a previous beam region has shifted, since the 3.7 μs long oscillations have been unexpected.

Chapter 6

Temperature measurement

This chapter investigates the effect of varying temperature inside of the Bunch Arrival Monitor on the arrival time measurement and presents a new design of a pin header board for the TEC controller board, described in section 4.2.4. Temperature fluctuations cause timing drifts in optical fibers and shift the working point of the EOMs. For precise arrival time measurement, the Electro-Optical unit housing all the timing-critical components, i. e. the optics, fibre-optics, DC and RF electronic devices, is mounted inside a thermally insulated compartment with actively stabilized environmental conditions. The case is separated into a lower compartment with larger heat load components, such as TMCB, LDD, TEC controller and radiators of peltier elements, and a thermally insulated upper compartment. The front area of the upper compartment, accommodating the optical delays, utilizes passive temperature stabilization while the temperature of the rear, accommodating sensitive fibre-optics and RF components, is actively stabilized. [29] The two compartments housing the corresponding components are displayed in Fig. 4.3.

6.1 Methodology

The TEC controller, described in section 4.2.4, inside the BAM box was controlled remotely via the EuXFEL Java Data Display program for the Distributed Object Oriented Control System [33]. Arrival time data was extracted from three BAM stations, the 414.B2 station which is located 414 m from the photinjector, and the 1932M.TL and 1932S.TL stations which are located 1932 m from the photoinjector and less than a meter apart from

25

each other. The temperature was increased from 25 °C to 26° C by 0.1 °C, until the temperature has stabilized at the given value, at the 1932M.TL BAM station. The 414.B2 and the 1932S.TL were kept at a stable temperature of 25 °C all the time. Arrival time data was extracted using the pyDOOCS library and stored in an h5py file. First, absolute arrival time of the bunches inside the 4.5 MHz filled bunch-trains is read using the function pydoocs.read(), then, for the same macropulse of all three BAM stations, up to 1000 non-zero bunches inside of the 4.5 MHz filled bunch-train are stored every tenth of a second. After one hour the resulting data file should contain a 36 000×1000 array, where the rows contain the non-zero bunches in a bunch-train. The h5py file then contains arrival times of all three stations, their macropulse numbers and temperatures.

■ 6.2 **Results**

Every measured bunch-train macropulse contained 557 non-zero bunches. For every temperature value 100 bunch-trains were analyzed. The mean arrival time was calculated for all 100 bunch-trains. The first of these 100 mean arrival time values for all temperatures and stations is shown in Fig. 6.1. The timing jitter was calculated as a standard deviation of the 100 mean arrival time values, and is shown for all temperatures and stations in Fig. 6.2.

The mean arrival time values of the 100 bunch-trains for station 1932S.TL were subtracted from the values for station 1932M.TL for all temperatures to obtain an offset between these two stations. These offset values were then fitted by a linear function $f(T) = aT + b$. The fit was calculated using the nonlinear least-squares Marquardt-Levenberg algorithm in Gnuplot, and the parameters of the fit are displayed in Table 6.1.

Ndf	9
χ^2_ν	0.07
p	$> .999$
a	$-(173 \pm 9)$ K·fs^{-1}
b	(4.7 ± 0.2) ps

Table 6.1: Fit parameters of the linear fit $f(T) = aT + b$, where $f(T)$ is the arrival time in femtoseconds as a function of temperature T in Kelvin. Ndf is the number of degrees of freedom, χ^2_ν is the reduced chi-square of the fit and p is the p-value of the chisquare-distribution.
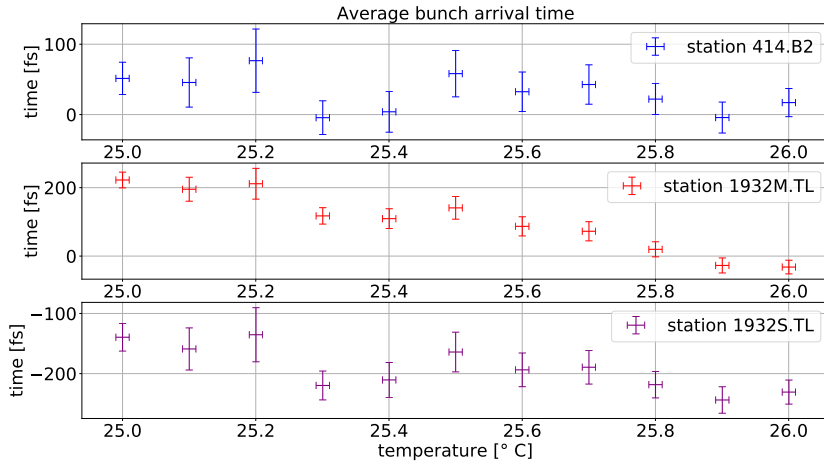
Figure 6.1: Average bunch arrival time inside the bunch-train for different temperatures and BAM stations.

6.3 Discussion

The parameter $a = -(173 \pm 9)$ fs $\cdot$ K^{-1} describes the change in measured arrival time on the varying temperature. As is seen from Fig. 6.1, the timing jitter does not depend on the varying temperature, and is around 20–45 fs for all BAM stations. The measured arrival time decreases with increasing temperature mainly due to timing drifts in optical fibers and shifting of the working point of the EOMs, as mentioned in the beginning of this chapter. The optical fibers inside the Electro-Optical unit are approximately 5 meters long which gives a timing drift value of approximately 35 fs $\cdot$ K^{-1} $\cdot$ m^{-1}, which is in the typical range for optical fibers according to [29]. The small value of residual variance $\chi^2_\nu = 0.07$ suggests that the errors of the fitted data, shown in Fig. 6.3, are too large. These errors are, however, caused by random arrival time fluctuations and can not be reduced substantially. To improve the accuracy of the measurement, more temperature values may be investigated, and longer thermal stabilization realised.

6.4 TEC pin header PCB design

The TEC controller has a high temperature control precision of up to 0.001 K, and communicates remotely through the digital pins of the TMCB. A new design of digital pin header connected to a terminal block is proposed

27
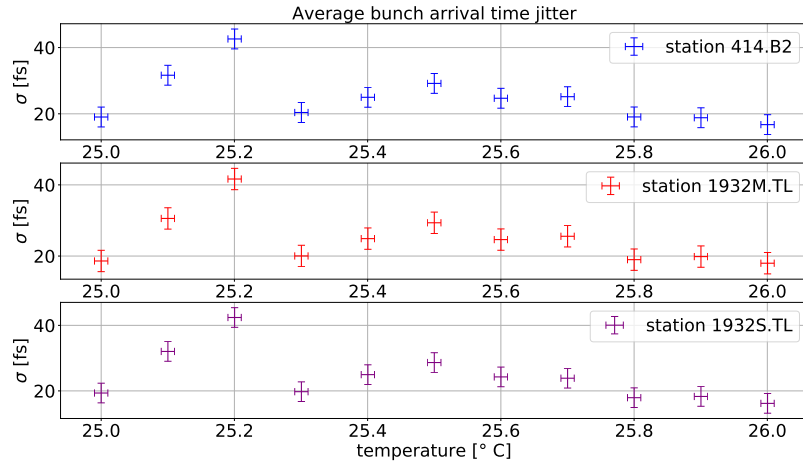
Figure 6.2: Average bunch arrival time jitter of the 100 bunch-trains for different temperatures and BAM stations.

here in order to reduce the difficulty of replacing the controller after hardware failure, and to introduce a series resistance for resonance damping due to high residual capacitance and inductance inside cables. The TEC pinout is connected to the pin header P1, which is connected to a terminal block J1. The voltage input is connected from the pin header to the terminal block via a resistor R1 with resistance of 5 mΩ. The resistor has to handle voltage of up to 24 V and current of 2 A. The 3D view PCB board, designed in Altium Nexus, is depicted in Fig 6.4.
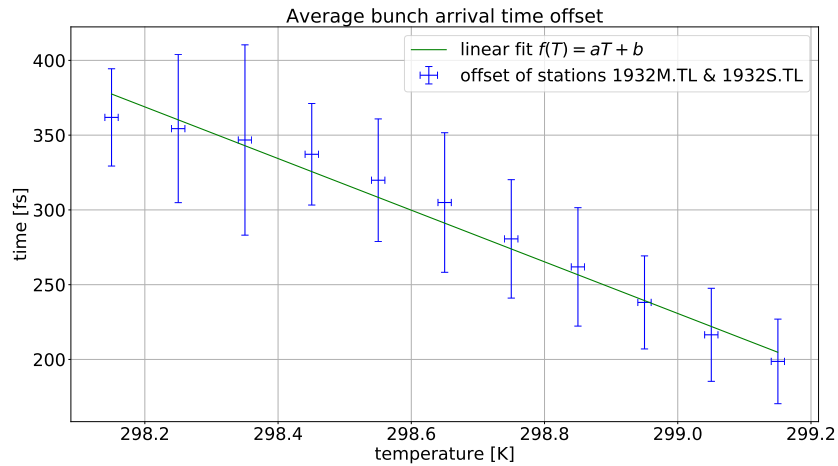
Figure 6.3: Offset of average bunch arrival time between the stations 1932M.TL and 1932S.TL for different temperatures and a linear fit $f(T) = aT + b$ with parameters $a = -(173 \pm 9)$ fs $\cdot$ K^{-1}, $b = (4.7 \pm 0.2)$ ps, where $f(T)$ is the arrival time in femtoseconds as a function of temperature T in Kelvin. The fit was calculated using the nonlinear least-squares Marquardt-Levenberg algorithm in Gnuplot, and the parameters of the fit are displayed in Table 6.1.
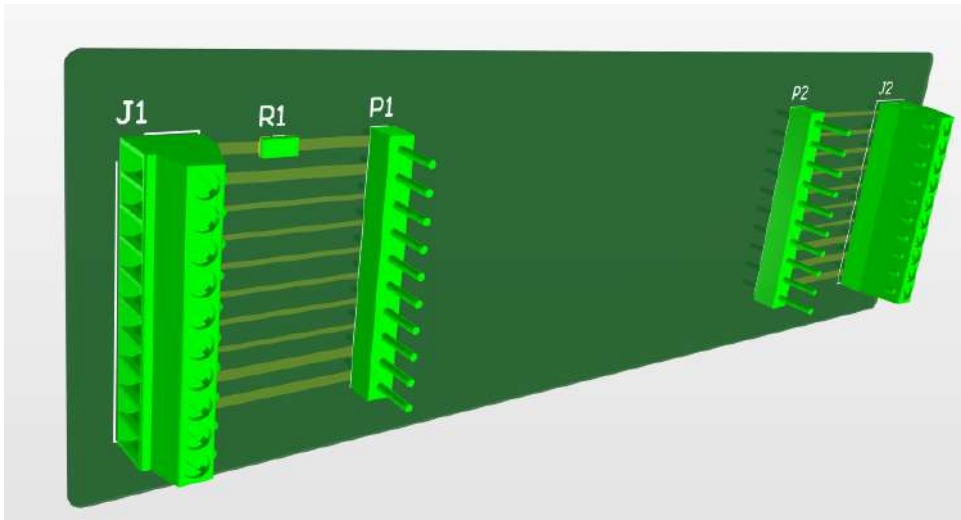
Figure 6.4: PCB board designed in Altium Nexus for the TEC controller pinout P1 connected to a terminal block J1. The voltage input is connected from the pin header to the terminal block via a resistor R1.

29

Chapter 7

Humidity measurement

This chapter investigates humidity variations in the BAMs and their effect on arrival time measurement. Relative humidity variations also affect the timing-critical components inside the Electro-Optical unit, such as fibre-optics and electronic devices, mentioned in previous chapter. First, calibration of the humidity sensor[1] was performed.

7.1 Humidity sensor calibration

The humidity sensor, shown in Fig. 7.1, is connected to a fixed-output voltage regulator IC[2], which provides a stable voltage supply of 5 V. Two humidity sensors were put inside of a bench-top type temperature and humidity climatic chamber. The output voltage regulator IC was powered by an external voltage supply of 5.8 V and 8 mA current, shown on top of the climate chamber in Fig. 7.2 next to a digital multimeter. The sensors were connected to a TMCB, described in section 4.2.4, through an analog input connector, which allowed to read the signal from their respective ADC channels via an Ethernet cable connected to a laptop. To read the signal from the humidity sensors, firmware was installed to a FPGA register of the TMCB via a bit file.

The signal voltage output of the sensor was also read using a digital multimeter. The climate chamber was kept at temperature of around

---

[1] Honeywell HIH-4001 Series
[2] LM7805

31

Figure 7.1: The Honeywell HIH-4001 humidity sensor connected to the LM7805 fixed-output voltage regulator IC. The regularor is supplied by voltage V_{in} and the sensor outputs voltage V_{out}.

T = (25.3 ± 0.6) °C and the humidity was controlled via the panel of the chamber.

The 16 bit ADC samples analog input voltage in the –10 V to 10 V range. Therefore the voltage output V_{out} of the analog signal can be obtained from the equation

$$V_{out} = \frac{ADC}{2^{15} - 1} \cdot 10 \text{ V}, \tag{7.1}$$

where ADC represents the signed output data from the ADC register. The relative humidity RH values set inside the chamber, the voltage V read by the digital multimeter, the ADC sample data and voltage output V_{ADC} calculated using equation (7.1), together with the total voltage output V_{out} taken as a weighted average of V and V_{ADC} for the two humidity sensors are shown in Table 7.1 and Table 7.2. The relation between the relative humidity RH inside the climate chamber and the voltage output V_{out} values of both sensors divided by the voltage input V_{in} of 5 V, provided by the fixed output voltage regulator IC, is shown in Fig. 7.3. These values were fitted by a linear function $f(\frac{V_{out}}{V_{in}}) = a\frac{V_{out}}{V_{in}} + b$, from which the calibration curve for the humidity sensors, also shown in Fig. 7.3, was obtained. The fit was calculated using the nonlinear least-squares Marquardt-Levenberg algorithm in Gnuplot, and the fit parameters are displayed in Table 7.3.

Figure 7.2: Bench-top type temperature and humidity chamber, an external voltage power supply on top together with a digital multimeter on right.

7.2 Humidity monitoring

The relative humidity was monitored over 24 hour period at BAM stations FL0.UBC2 and FLF.MAFF at FLASH and over a 12 hour period at stations 414.B2, 1932M.TL and 1932S.TL at EuXFEL. Average relative humidity RH for the FLASH BAM stations was calculated using a 5 minute long moving average sliding window, and is shown in Fig. 7.4. A 10 minute long moving average sliding window was used to calculate the average relative humidity RH for the EuXFEL BAM stations, which is shown in Fig. 7.5. From Fig. 7.4 and Fig. 7.5 it can be seen that, despite having distinct values, the relative humidity changes similarly for the different BAM stations inside the ventilated accelerator tunnel.

Fig. 7.6 shows the standard deviation of average bunch arrival time inside of the macropulse bunch-train for the EuXFEL BAM stations, calculated analogously to the timing jitter for different temperatures in section 6.2. The timing jitter seems to not change with different relative humidity and is around 25–50 fs for all BAM stations at the EUXFEL. The relation between

RH [%]	V [V]	ADC [-]	V_{ADC} [V]	V_{out} [V]
26	1.44	4600	1.40	1.44
30	1.54	4900	1.50	1.54
41	1.93	6200	1.89	1.93
51	2.22	7100	2.17	2.21
60	2.62	8300	2.53	2.61
70	2.87	9200	2.81	2.86

Table 7.1: The voltage *V* read by the multimeter with precision of ±0.01 V, the dimensionless ADC data samples read with precision of ±50 samples, the voltage V_{ADC} calculated from equation (7.1) with uncertainty of ±0.03 V and the total voltage output V_{out} taken as a weighted average of *V* and V_{ADC} with uncertainty of ±0.03 V for a relative humidity RH set with precision of ±1% inside the climate chamber for the first humidity sensor.

RH [%]	*V* [V]	ADC [-]	V_{ADC} [V]	V_{out} [V]
35	1.63	5000	1.53	1.62
40	1.75	5500	1.68	1.74
45	1.92	6100	1.86	1.91
51	2.36	7600	2.32	2.36
58	2.40	8000	2.44	2.40
68	2.80	8900	2.72	2.79

Table 7.2: The voltage *V* read by the multimeter with precision of ±0.01 V, the dimensionless ADC data samples read with precision of ±50 samples, the voltage V_{ADC} calculated from equation (7.1) with uncertainty of ±0.03 V and the total voltage output V_{out} taken as a weighted average of *V* and V_{ADC} with uncertainty of ±0.03 V for a relative humidity RH set with precision of ±1% inside the climate chamber for the second humidity sensor.

arrival time measurement and relative humidity inside of a BAM could not be determined due to small humidity variation.

Ndf	10
χ^2_ν	5.02
p	$< .0001$
a	(1.44 ± 0.07)
b	$-(13 \pm 3)$ %

Table 7.3: Fit parameters of the humidity sensors' calibration curve $f(\frac{V_{\text{out}}}{V_{\text{in}}}) = a\frac{V_{\text{out}}}{V_{\text{in}}} + b$, where $f(\frac{V_{\text{out}}}{V_{\text{in}}})$ is the relative humidity RH given as a function of the ratio between the voltage output V_{out} and voltage input V_{in} of the humidity sensor. Ndf is the number of degrees of freedom, χ^2_ν is the reduced chi-square and p is the p-value of the chisquare-distribution.
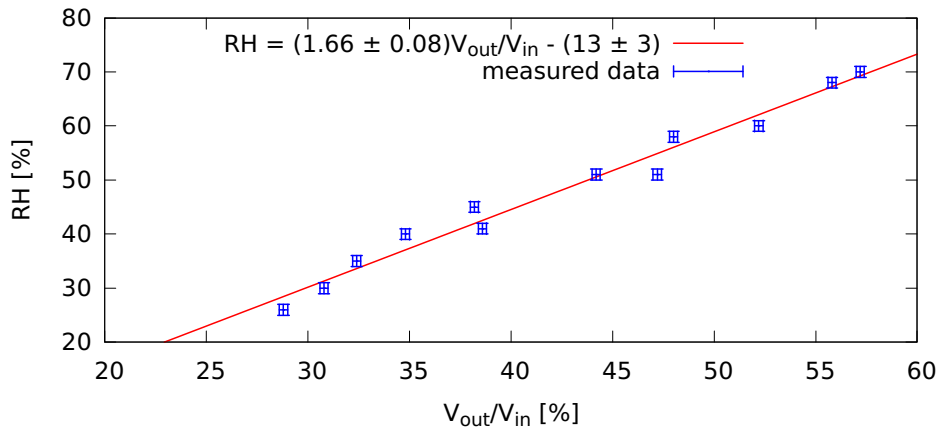
Figure 7.3: Measured data and calibration curve $f(\frac{V_{\text{out}}}{V_{\text{in}}}) = a\frac{V_{\text{out}}}{V_{\text{in}}} + b$ with parameters $a = (1.44 \pm 0.07)$ and $b = -(13 \pm 3)$ %, where $f(\frac{V_{\text{out}}}{V_{\text{in}}})$ is the relative humidity RH given as a function of the ratio between the voltage output V_{out} and voltage input V_{in} of the humidity sensor. The fit was calculated using the nonlinear least-squares Marquardt-Levenberg algorithm in Gnuplot, and the fit parameters are displayed in Table 7.3.
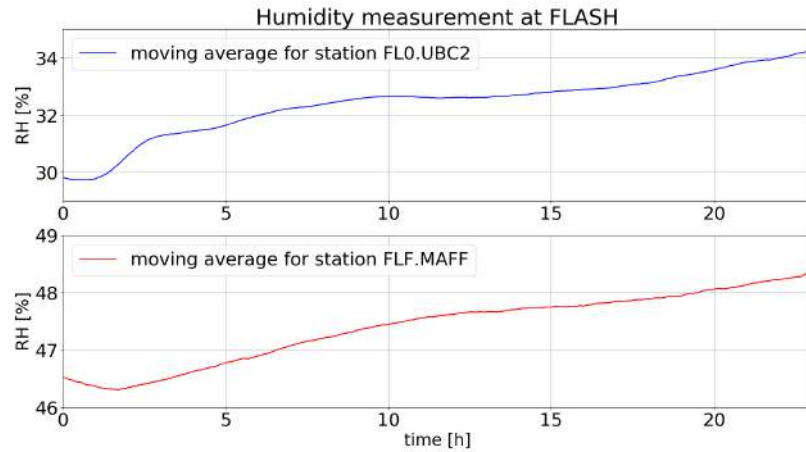
Figure 7.4: Average relative humidity RH for the FLASH FL0.UBC2 and FLF.MAFF BAM stations calculated using a 5 minute long moving average sliding window over a 24 hour period.
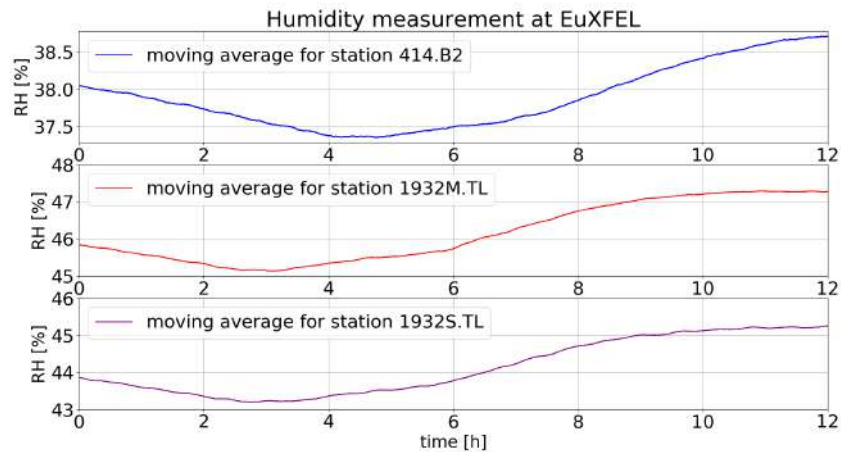

Figure 7.5: Average relative humidity RH for the EuXFEL 414.B2, 1932M.TL and 1932S.TL BAM stations calculated using a 10 minute long moving average sliding window over a 12 hour period.
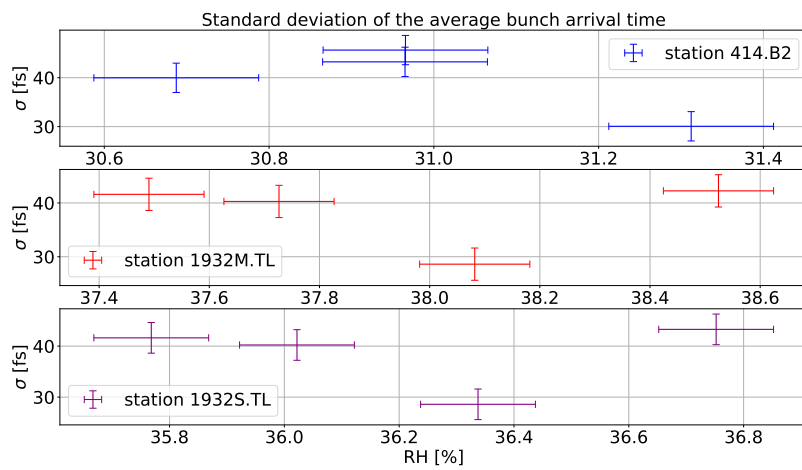
Figure 7.6: Average bunch arrival time jitter of the 100 bunch-trains for different relative humidity RH values and BAM stations at EuXFEL.

Chapter 8

Summary

The aim of this project was to describe the precise arrival time measurement of the electron bunches inside the superconducting linear accelerators of FLASH and EuXFEL at DESY, and explain why it is needed, in addition to determining the effect of environmental conditions, i.e. temperature and humidity variations, on this measurement, and especially on the fiber-optic chain.

The first three chapters contained a theoretical overview of accelerators, Free-Electron Lasers and Bunch Arrival Monitors. An overview of accelerator physics, development and instrumentation was given in Chapter 2. The working principle of Free-Electron Lasers, their development and bunch compressors were described in Chapter 3 while Chapter 4 focused on the components and operation of Bunch Arrival Monitors.

Chapters 5, 6 and 7 focused on the practical part of this project. Chapter 5 investigates the influence of noise induced by optical switch on the BAM signal computation algorithm. The noise influences around 800 ADC samples, corresponding to 3.7 μs, which is smaller than the typical transition period of beam regions. Therefore the noise induced by the optical switch does not affect the arrival time of bunches measured in different beam regions computed by the BAM signal algorithm.

The relation between temperature variations and bunch arrival measurement was established in Chapter 6. The measured arrival time decreases with increasing temperature by (173 ± 9) fs $\cdot$ K^{-1}, which corresponds to a timing drift value of approximately 35 fs $\cdot$ K^{-1} $\cdot$ m^{-1} inside the fiber-optics while

the timing jitter does not change. New design of a pin header PCB for a Thermo-Electric Cooling (TEC) Temperature Controller was also given in Chapter 6.

Chapter 7 described the relative humidity fluctuations inside the BAMs. Calibration curve of the humidity sensor was calculated and is shown in Fig. 7.3. The timing jitter seems to not change with varying temperature. The dependence of the absolute arrival time measurement on relative humidity has not been yet established.

Future outlooks for this project include improving the TEC controller pin header PCB board design and its implementation, and quantifying the affect of humidity variations on the arrival time measurement, in addition to improving the accuracy of the temperature measurement.

Appendix A

Bibliography

[1] Jörg Rossbach, Jochen R. Schneider, and Wilfried Wurth. "10 years of pioneering X-ray science at the Free-Electron Laser FLASH at DESY". In: *Physics Reports* 808 (2019). 10 years of pioneering X-ray science at the Free-Electron Laser FLASH at DESY, pp. 1–74. ISSN: 0370-1573. DOI: https://doi.org/10.1016/j.physrep.2019.02.002.

[2] Stephen Myers and Oliver Bruning. *Challenges and Goals for Accelerators in the 21st century.* 5 Toh Tuck Link, Singapore 596224: World Scientific Publishing Co. Pte. Ltd., 2016, pp. 28, 36–39. ISBN: 978-9814436397.

[3] M. Vretenar. "Radio frequency for particle accelerators: evolution and anatomy of a technology". In: *CERN Accelerator School: Course on RF for Accelerators.* Jan. 2012, pp. 1–14. arXiv: 1201.2345 [physics.acc-ph].

[4] P. J. Bryant. "A Brief history and review of accelerators". In: *CERN Accelerator School: Course on General Accelerator Physics.* Vol. 2. 1992, pp. 1–16.

[5] Andrew Sessler and Edmund Wilson. *Engines of discovery.* 5 Toh Tuck Link, Singapore 596224: World Scientific Publishing Co. Pte. Ltd., 2014, pp. 2, 5–8. ISBN: 978-981-4417-18-1.

[6] Shyh-Yuan Lee. *Accelerator physics.* Fourth. 5 Toh Tuck Link, Singapore 596224: World Scientific Publishing Co. Pte. Ltd., 2019, pp. 8–10, 17–18. ISBN: 978-981-3274-67-9.

[7] Alexander Wu Chao et al. *Handbook of Accelerator Physics and Engineering.* Second. 5 Toh Tuck Link, Singapore 596224: World Scientific Publishing Co. Pte. Ltd., 2013, pp. 58–59, 229, 334–335. ISBN: 978-981-4415-84-2.

[8]   R. Appleby et al. *The Science and Technology of Particle Accelerators.* First. Boca Raton: CRC Press, 2020, pp. 1–6, 23–24. DOI: `10.1201/9781351007962`.

[9]   Alexander Wu Chao et al. *Handbook of Accelerator Physics and Engineering.* Third. 5 Toh Tuck Link, Singapore 596224: World Scientific Publishing Co. Pte. Ltd., 2023, pp. 89–93. ISBN: 978-981-126-917-2.

[10]   Michael Barnes. "Kicker systems". In: *CERN Yellow Rep. School Proc.* 5 (2018). Ed. by Bernhard Holzer, p. 229. DOI: `10.23730/CYRSP-2018-005.229`.

[11]   Peter Forck, P. Kowina, and Dmitry Liakin. "Beam position monitors". In: *CAS - CERN Accelerator School: Course on Beam Diagnostics.* Aug. 2009, pp. 187–228. ISBN: CERN–2009–005.

[12]   Kay Wittenburg. "Beam loss monitors". In: *CAS 2008 - CERN Accelerator School: Beam Diagnostics, Proceedings.* May 2008, pp. 249–280.

[13]   J.-C. Denard. "Beam current monitors". In: 2009, pp. 141–155. URL: `https://cds.cern.ch/record/1213275/files/p141.pdf`.

[14]   D. A. Edwards and M. J. Syphers. *An Introduction to the Physics of High-Energy Accelerators.* Wiley Series in Beam Physics and Accelerator Technology. New York: Wiley, 1992, pp. 7–8. ISBN: 978-0-471-55163-8.

[15]   P. Schmüser and DESY. "Free-Electron Lasers". In: DESY Summer Students Program, Hamburg (Germany), 26 Jul 2006 - 1 Sep 2006. July 26, 2006. URL: `https://bib-pubdb1.desy.de/record/80632`.

[16]   K Tiedtke et al. "The soft x-ray free-electron laser FLASH at DESY: beamlines, diagnostics and end-stations". In: *New Journal of Physics* 11.2 (2009), p. 023029. DOI: `10.1088/1367-2630/11/2/023029`.

[17]   M. V. Kovalchuk and A. E. Blagov. "European X-ray Free-Electron Laser". In: *Crystallography Reports* 67 (2022), pp. 631–675. DOI: `10.1134/S1063774522050066`.

[18]   John M. J. Madey. "Stimulated Emission of Bremsstrahlung in a Periodic Magnetic Field". In: *J. Appl. Phys.* 42 (1971), pp. 1906–1913. DOI: `10.1063/1.1660466`.

[19]   W. Ackermann et al. "Operation of a free-electron laser from the extreme ultraviolet to the water window". English. In: *Nature Photonics* 1.6 (July 2007), pp. 336–342. ISSN: 1749-4885. DOI: `10.1038/nphoton.2007.76`.

[20]   W. Decking et al. "A MHz-repetition-rate hard X-ray free-electron laser driven by a superconducting linear accelerator". In: *Nature Photonics* 14 (June 2020), pp. 391–397. DOI: `10.1038/s41566-020-0607-z`.

[21]   Marie Czwalinna et al. "Beam Arrival Stability at the European XFEL". In: *12th International Particle Accelerator Conference.* Aug. 2021. DOI: `10.18429/JACoW-IPAC2021-THXB02`.

[22]   F. Löhl et al. "Electron Bunch Timing with Femtosecond Precision in a Superconducting Free-Electron Laser". In: *Phys. Rev. Lett.* 104 (14 2010), p. 144801. DOI: 10.1103/PhysRevLett.104.144801.

[23]   Simone Di Mitri. "Bunch Length Compressors". In: *CERN Yellow Rep. School Proc.* 1 (2018). Ed. by R. Bayley, pp. 363–380. DOI: 10.23730/CYRSP-2018-001.363.

[24]   S Schulz et al. "Femtosecond all-optical synchronization of an X-ray free-electron laser". In: *Nature communications* 6 (Jan. 2015), p. 5938. DOI: 10.1038/ncomms6938.

[25]   Michele Viti et al. "The Bunch Arrival Time Monitor at FLASH and European XFEL". In: *Proceedings, 16th International Conference on Accelerator and Large Experimental Physics Control Systems (ICALEPCS 2017) : Barcelona, Spain, October 8-13, 2017.* 2018, pp. 701–705. DOI: 10.18429/JACoW-ICALEPCS2017-TUPHA125.

[26]   *Data Structure - MSK SDiag Public - DESY Confluence*. URL: https://confluence.desy.de/display/SDiagPublic/BAM+Data+Structure.

[27]   B. E. J. Scheible et al. "Pickup development for short low-charge bunches in x-ray free-electron lasers". In: *Phys. Rev. Accel. Beams* 24 (7 2021), p. 072803. DOI: 10.1103/PhysRevAccelBeams.24.072803.

[28]   Jin-Guo Wang et al. "Analysis of electro-optical intensity modulator for bunch arrival-time monitor at SXFEL". In: *Nuclear Science and Techniques* 30 (1 Jan. 2019), pp. 2210–3147. DOI: 10.1007/s41365-018-0524-8.

[29]   Hannes Dinter et al. "Prototype of the Improved Electro-Optical Unit for the Bunch Arrival Time Monitors at FLASH and the European XFEL". In: *Proceedings, 37th International Free Electron Laser Conference (FEL 2015) : Daejeon, Korea, August 23-28, 2015.* 2015, pp. 478–478. DOI: 10.18429/JACoW-FEL2015-TUP049.

[30]   Aleksandar Angelovski et al. "Evaluation of the cone-shaped pickup performance for low charge sub-10 fs arrival-time measurements at free electron laser facilities". In: *Phys. Rev. ST Accel. Beams* 18 (1 2015), p. 012801. DOI: 10.1103/PhysRevSTAB.18.012801.

[31]   M. Diomede et al. *Update on the LLRF operations status at the European XFEL*. Oct. 2022. arXiv: 2210.04711 [physics.acc-ph].

[32]   K. Przygoda et al. "MICROTCA.4 BASED OPTICAL FRONTEND READOUT ELECTRONICS AND ITS APPLICATIONS". In: *5th International Beam Instrumentation Conference*. Oct. 2017, pp. 67–70. ISBN: 978-3-95450-193-9. DOI: 10.18429/JACoW-IBIC2016-MOPG13.

[33]   Elke Sombrowski, Raimund Kammering, and Kay Rehlich. "A HTML5 Web Interface for JAVA DOOCS Data Display". In: *15th International Conference on Accelerator and Large Experimental Physics Control Systems*. 2015, pp. 1056–1058. ISBN: 978-3-95450-148-9. DOI: 10.18429/JACoW-ICALEPCS2015-WEPGF150.